

# Radial stellar populations of AGN-host dwarf galaxies in SDSS-IV MaNGA survey

Wei Cai<sup>1,2,3</sup>, Yinghe Zhao<sup>1,3,4\*\*</sup> and Jin-Ming Bai<sup>1,3,4</sup>

<sup>1</sup> Yunnan Observatories, Chinese Academy of Sciences, Kunming 652016, China;

*zhaoyinghe@ynao.ac.cn*

<sup>2</sup> University of Chinese Academy of Sciences, Beijing 100049, China

<sup>3</sup> Key Laboratory for the Structure and Evolution of Celestial Objects, Chinese Academy of Sciences, Kunming 650216, China

<sup>4</sup> Center for Astronomical Mega-Science, Chinese Academy of Sciences, Beijing 100012, China

Received 20xx month day; accepted 20xx month day

**Abstract** Based on MaNGA integral field unit (IFU) spectroscopy we search 60 AGN candidates, which have stellar masses  $M_{\star} \leq 5 \times 10^9 M_{\odot}$  and show AGN ionization signatures in the BPT diagram. For these AGN candidates, we derive the spatially resolved stellar population with the stellar population synthesis code STARLIGHT and measure the gradients of the mean stellar age and metallicity. We find that the gradients of mean stellar age (metallicity) of individual AGN-host dwarfs are diverse in  $0-0.5 Re$ ,  $0.5-1 Re$  and  $0-1 Re$ . However, the overall behavior of the mean stellar age (metallicity) profiles tend to be flat, as the median values of the gradients are close to zero. We further study the overall behavior of the mean stellar age (metallicity) by plotting the co-added radial profiles for the AGN sample and compare with a control sample with similar stellar mass. We find that the median values of light-weighted mean stellar ages of AGN sample are as old as  $2-3$  Gyr within  $2 Re$ , which are about  $4-7$  times older than those of the control sample. Meanwhile, most of the AGN candidates are low-level AGNs, as only eight sources have  $L_{[\text{O III}]} > 10^{39.5} \text{ erg s}^{-1}$ . Hence, the AGNs in dwarf galaxies might accelerate the evolution of galaxies by accelerating the consumption of the gas, resulting in an overall quenching of the dwarf galaxies, and the AGNs also become weak due to the lack of gas. The median values of mass-weighted mean stellar age of both samples within  $2 Re$  are similar and as old as about 10 Gyr, indicating that the stellar mass is mainly contributed by old stellar populations. The gradients of co-added mean stellar metallicity for both samples tend to be negative but close to zero, and the similar mean stellar metallicity profiles for both samples indicate that the chemical evolution of the host galaxy is not strongly influenced by the AGN.

\*\* Author to whom any correspondence should be addressed

**Key words:** galaxies: dwarf - galaxies: active - galaxies: galaxies stellar content

## 1 INTRODUCTION

The relation between the mass of supermassive black holes (SMBHs) and bulge stellar velocity dispersion (the  $M_{\star} - \sigma$  relation) suggests that the growth of central SMBHs is coupled with the growth of host galaxies (e.g., Ferrarese & Merritt 2000; Gebhardt et al. 2000; Kormendy & Ho 2013). This relation has been explained by active galactic nuclei (AGN) feedback process that AGNs regulate the star formation of host galaxies in both radiative and kinetic forms (e.g., Fabian 2012), which might heat the gas, or even expel the gas from the galaxy. Indeed, the feedback mechanisms such as AGNs (e.g., Bower et al. 2006; Schaye et al. 2015; Terrazas et al. 2020) must be included in cosmological models to regulate star formation of the massive galaxies. Therefore, AGN effects on the evolution of massive galaxies have been widely accepted (see the reviews by Heckman & Best 2014).

AGNs have also been found in low-mass, dwarf galaxies (e.g., NGC 4395; Filippenko & Sargent 1989; POX 52; Barth et al. 2004). In recent years, more and more dwarf galaxies with clear AGN signatures are identified at all wavelength from X-ray to radio band (e.g., Reines et al. 2013; Moran et al. 2014; Lemons et al. 2015; Sartori et al. 2015; Mezcua et al. 2019; Birchall et al. 2020; Reines et al. 2020). The central BHs in dwarf galaxies are suggested to be intermediate-mass black holes (IMBHs) with mass between  $10^2$  and  $10^6 M_{\odot}$  (e.g., Reines et al. 2013; Moran et al. 2014; Silk 2017), which might have similar mass with the first seed black holes due to the relatively quiet merger histories of dwarf galaxies (Bellovary et al. 2011). Furthermore, dwarf galaxies have similar conditions of high-redshift galaxies due to their low metallicity (e.g., Mateo 1998). Therefore, it's essential to investigate the AGN effects on the dwarf galaxies, which could improve our understanding of AGN role in galaxy formation and evolution.

In recent years, a series of works have studied the AGN effects on the evolution of dwarf galaxies, while the importance of AGNs in regulating the star formation of dwarf galaxies is still in debate. Some works suggest that AGNs should have strong effects on the star formation of dwarf galaxies (e.g., Dashyan et al. 2018; Penny et al. 2018; Barai & de Gouveia Dal Pino 2019; Manzano-King et al. 2019; Mezcua et al. 2019; Sharma et al. 2020). However, other works (e.g., Trebitsch et al. 2018; Koudmani et al. 2019) propose that AGN effects on regulating the star formation of host galaxies are negligible.

AGN is expected to have connection with the stellar population of host galaxy. AGN may be triggered when the nuclear engine is being fed by the inflow of material, which could also be used to form new stars. AGN feedback might also influence the stellar population of host galaxy by regulating the star formation. A number of works have studied the stellar populations of AGN-host massive galaxies by using both central spectra (e.g., Cid Fernandes et al. 2004; hereafter C04) and IFU spectra (e.g., Sánchez et al. 2018; Mallmann et al. 2018) and suggested that nuclear activities might be relevant to recent episodes of circumnuclear star formation (e.g., Storchi-Bergmann et al. 2001; Rembold et al. 2017). In AGN-host dwarfs, our work (Cai et al. 2020) presents a detailed study of the stellar populations for a sample containing 136 sources and shows a diversity of SFHs for these optically selected AGN-host dwarfs. We further find a mild correlation between the SFHs and the luminosity of the [O III]  $\lambda 5007$  line ( $L_{[\text{O III}]}$ ) for sources with  $L_{[\text{O III}]} > 10^{39}$  erg s $^{-1}$ , indicating a physical connection between star formation and AGN activities.

However, the stellar populations of the AGN-host dwarfs in [Cai et al. \(2020\)](#) are limited to the central regions using the spectra observed from a  $3''$ -diameter aperture. In recent years, the IFU technology has been developed and the integral-field spectroscopy can provide us a wealth of information for each individual galaxy (such as the spatially resolved stellar populations, which can be used to locate the sites of new and recent star formation), which can improve our understanding of the evolution of galaxies and reveal the possible quenching mechanisms. The spatial distribution of the stellar ages, element abundances, and star formation histories (or the gradients of these parameters) can reveal how galaxy grows or quenches. Many works have studied the age and metallicity gradients for both disc and elliptical galaxies, and most of their works (e.g., [González Delgado et al. 2015](#); [Morelli et al. 2015](#); [Zheng et al. 2017](#)) find a negative gradient, indicating inside-out growth of galaxies. However, the outside-in mode has been suggested in many nearby dwarf galaxies (e.g., [Zhang et al. 2012](#)), and a negative correlation is found between the stellar population gradients and the stellar mass (e.g., [Chen et al. 2020](#)). A series of works (e.g., [Zheng et al. 2017](#); [Chen et al. 2020](#)) have also found no/weak correlation between the age (metallicity) gradients and the local density environment.

To further investigate the AGN effects on the SFHs of dwarf galaxies, in this paper we present our detailed studies on the radial stellar populations for a sample of 60 AGN-host dwarf galaxies, selected from the MaNGA survey. We further compare the results of AGN-host dwarfs with a control sample of carefully selected normal galaxies. The paper is organized as follows. Section 2 describes the basic informations of MaNGA data, the selection of the AGN and control samples and our data reductions. Our results and analysis are given in Section 3. We compare the properties of the AGN sample with those of control samples, the  $H\alpha$  equivalent width of the AGN sample in Section 4 and present our conclusions in the last section. Throughout this paper, we adopt a Hubble constant of  $H_0 = 70 \text{ km s}^{-1} \text{ Mpc}^{-1}$ ,  $\Omega_M=0.28$ , and  $\Omega_\Lambda=0.72$ , which are based on the five-year *WMAP* results ([Hinshaw et al. 2009](#)).

## 2 SAMPLE AND DATA ANALYSIS

### 2.1 Sample

MaNGA is the largest ongoing IFU survey, aiming to acquire spatially resolved spectra of 100 000 nearby galaxies ( $z < 0.1$ ) from 2014 to 2020 ([Bundy et al. 2015](#); [Law et al. 2015](#); [Blanton et al. 2017](#)). MaNGA target galaxies are selected from the NASA-Sloan Atlas (NSA) catalog <sup>1</sup> (version v1.0.1) with a flat distribution in the stellar mass above  $10^9 M_\odot$ . In addition, a small ancillary sample is observed to extend the MaNGA sample to lower mass. The MaNGA observations are carried out with 17 fiber-bundle IFUs with 5 different sizes, varying in diameter from  $12''$  (19 fibers) to  $32''$  (127 fibers). Galaxies are covered to at least 1.5 effective radii ( $Re$ ) in observation, where  $Re$  represents the radius containing 50% of the light of the galaxy measured at r-band. The observational spectrum has a spectral coverage ranging from  $3600 \text{ \AA}$  to  $10300 \text{ \AA}$  with a spectral resolution varying from  $R \sim 1400$  at  $4000 \text{ \AA}$  to  $R \sim 2600$  around  $9000 \text{ \AA}$  ([Drory et al. 2015](#); [Yan et al. 2016a,b](#)) provided by the dual beam BOSS spectrographs ([Smee et al. 2013](#)).

<sup>1</sup> <https://www.sdss.org/dr15/manga/manga-target-selection/nsa/>

The MaNGA parent sample used here is from the internal MaNGA Product Launch 6 (MPL 6) with 4718 galaxies observed within the first 4 years, corresponding to the SDSS data release 15<sup>2</sup>. The raw data were reduced, calibrated, and reconstructed to a data cube by the Data Reduction Pipeline (DRP) (Law et al. 2016). The final 3D data cubes deliver the spectra for each spaxel of a given galaxy and each spaxel has an area of  $0''.5 \times 0''.5$ .

### 2.1.1 AGN Sample

To select dwarf galaxies, we follow similar stellar mass limits as other work in the field (e.g., Reines et al. 2013; Penny et al. 2016, 2018), i.e.,  $M_* \leq 5 \times 10^9 M_\odot$ , corresponding roughly to the stellar mass of the Large Magellan Cloud. The stellar mass adopted here is derived with elliptical Petrosian fluxes (NSA.ELPETRO.MASS) from the MaNGA parent sample. There are about 900 dwarf galaxies in the MaNGA parent sample. We identify AGN candidates from this dwarf sample using the Baldwin, Phillips, & Telervich (BPT) diagram (e.g., Baldwin et al. 1981; Veilleux & Osterbrock 1987), which adopt the 2D line-intensity ratio calculated from relatively strong lines of  $H\beta$   $\lambda 4861$ ,  $[O\ III]$   $\lambda 5007$ ,  $H\alpha$   $\lambda 6563$ , and  $[N\ II]$   $\lambda 6584$  to probe the nebular conditions of a source. Mezcuca & Domínguez Sánchez (2020) have suggested that the AGN emission could be off-nuclear and the AGN emission might be overwhelmed by the light from its host galaxy when the integrated spectra are used. Therefore, for each dwarf galaxy, we construct the spatially resolved BPT diagram. Spaxels with signal-to-noise ratios (S/N) of the above four emission lines larger than 3 where are measured with the non-parametric emission line by MaNGA DAP, are used. A galaxy is considered as an AGN when the circumnuclear regions are classified as either the composite or the AGN. Finally, 49 AGN candidates are found by the spatially resolved BPT diagram, as shown in Figure 1.

Since we require all of the four lines having their  $S/N > 3$ , it might miss some AGNs using the spatially resolved BPT diagram. Therefore we bin the central  $1''.5$  radius spectra for each galaxy and model the stellar continuum using the STARLIGHT code (see Section 2.3). The pure emission line spectrum is obtained by subtracting the best-fit model spectrum from the observed one. We fit the emission lines with a Gaussian function, get the fluxes of  $H\alpha$ ,  $H\beta$ ,  $[O\ III]$ ,  $[N\ II]$ , and make use of the BPT diagram to classify the galaxy. Finally, 44 AGN-host galaxies (13 have AGN dominated spectra and 31 have composite spectra) are identified, as shown in Figure 2. The S/N of the four emission lines are all greater than 3 for these sources. There are 33 sources are overlapped between the central- $3''$  and spatially-resolved samples and thus the final sample contains 60 sources. We further checked the 16 AGNs which are classified as SF galaxies by using the central- $3''$  spectrum and found that most spaxels with AGN signature are off-nuclear. The existence of off-center AGNs are consistent with Bellovary et al. (2019) results, who have predicted that the wandering black holes are presented in dwarf galaxies, which might be attributed to the physical effects, such as interactions and mergers. However, these off-center AGNs might be not true off-center AGNs due to the star formation dilution in the center of the galaxy. It needs more data, such as X-ray, to further investigate the nature of these off-nuclear AGNs.

---

<sup>2</sup> <http://www.sdss.org/surveys/manga>

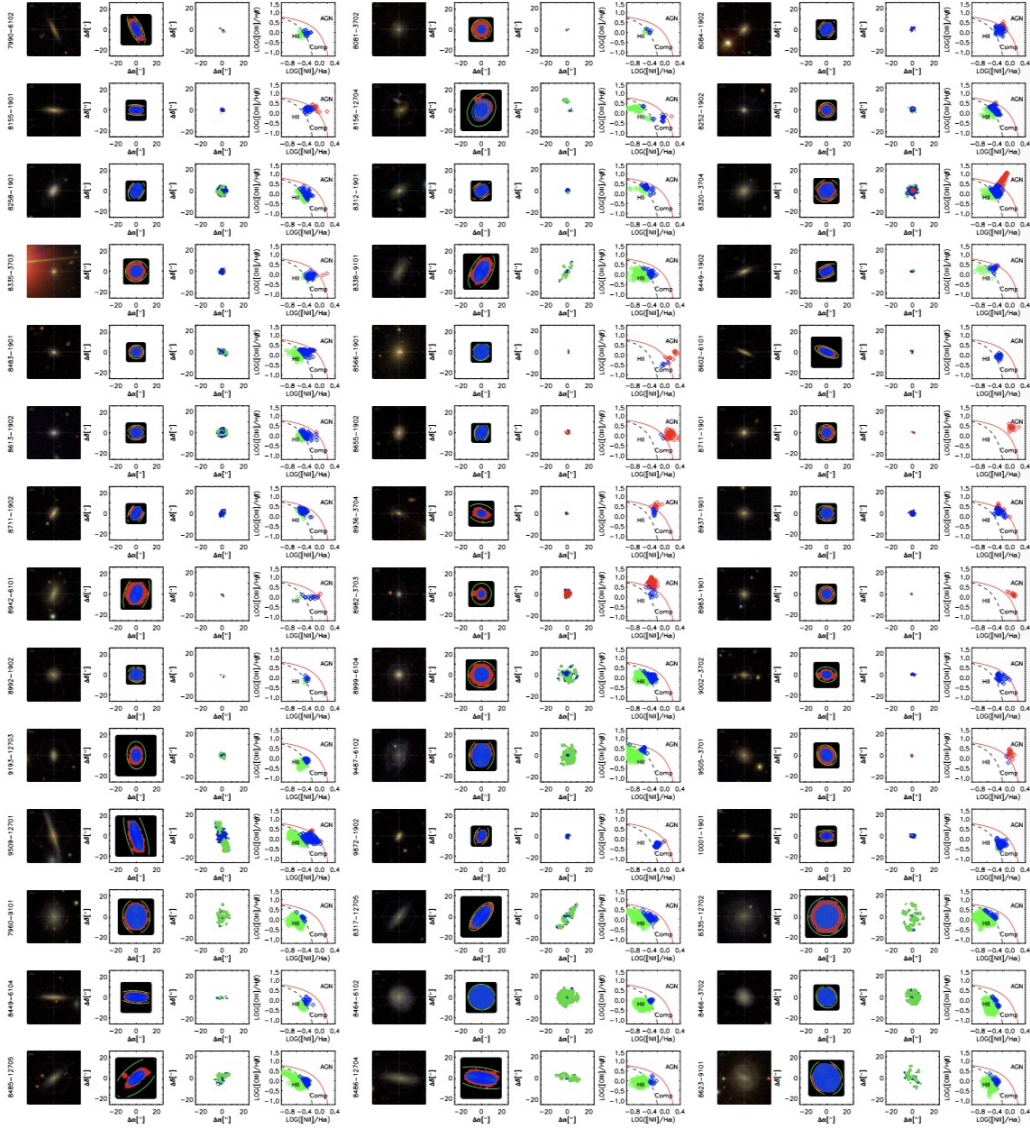


Fig. 1: The 49 AGN candidates identified by the spatially resolved BPT diagram. From left to right: the gri false-color images of AGN-host galaxies with MaNGA IFU footprint overlaid; The contour with the elliptical annuli we adopted to increase the S/N by binning the spectra. The blue elliptical annuli represent that the S/N is larger than 10, whereas the green elliptical annuli represent that the S/N is lower than 10 for the external regions of most galaxies; The BPT maps of AGN-host galaxies based on the emission line flux maps produced by MaNGA DAP; The BPT diagrams of AGN-host galaxies with different colors (AGNs (red), composite (blue) and star formation (green)) representing the ionization in different part of galaxies. The continuous lines separating AGNs, composite objects and star-forming galaxies are from [Kauffmann et al. \(2003\)](#) and [Kewley et al. \(2001\)](#).

In table 1, we show the properties for these AGN candidates. Four out of six AGN dwarf galaxies found by [Penny et al. \(2018\)](#) are included in our final AGN sample. One source (7815–1901) is not included because its mass is larger than  $5 \times 10^9 M_\odot$  and the another one (8623–9102) is caused by the different criterion in selecting the spaxels to construct the spatially resolved BPT diagram. Our AGN sample has a median redshift of  $\langle z \rangle = 0.025$ , a median  $g$ -band absolute magnitude of  $\langle M_g \rangle \sim -18.2$  mag, a median  $g-r$

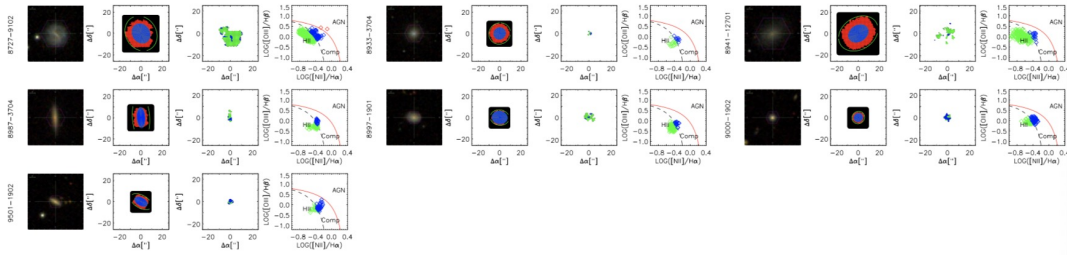


Fig. 1: Continued

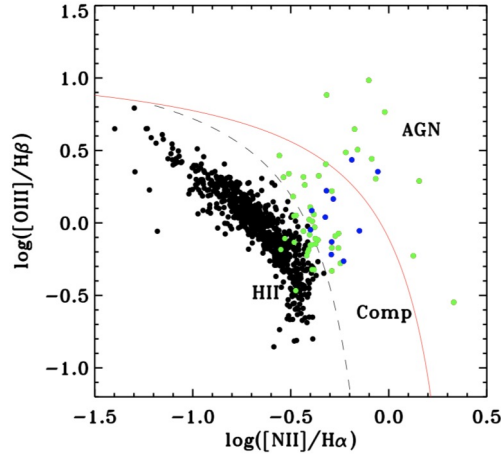


Fig. 2: BPT diagram for the dwarf galaxies using the emission lines fluxes from the pure central  $3''$  spectra. The continuous lines separating AGNs, composite objects and star-forming galaxies are from [Kauffmann et al. \(2003\)](#) and [Kewley et al. \(2001\)](#). Colored dots represent the 60 AGN candidates. Green dots represent the 49 AGN candidates identified by the spatially resolved BPT diagram.

color of  $\langle g - r \rangle = 0.58$  mag, and a median stellar mass of  $\langle M_{\star} \rangle = 3.5 \times 10^9 M_{\odot}$ . These properties of our AGN sample are similar to the larger AGN host dwarf galaxy sample in [Reines et al. \(2013\)](#). Meanwhile, as shown in Figure 3, we find that the distributions of galactic parameters of our AGN sample are similar to those of the parent sample, except for that few AGNs are found at the blue end. [Reines et al. \(2013\)](#) also found that their AGN sample selected by BPT diagram tends to be redder compared to the parent sample of dwarfs (see their Figure 7 for details). [Trump et al. \(2015\)](#) have suggested that AGN signature might be overwhelmed by the light from its host galaxy. Therefore, the redder color of AGN sample might be due to a selection bias arising from the optical diagnostics, which is not sensitive to AGNs in blue star-forming low-mass dwarf galaxies since the observed emission is dominated by galaxy light.

Table 1: Properties of the 60 AGN-host dwarf galaxies.

manga-Plateifu	manga-ID	Ra	Dec	$z$	$\log M_{\star}$	$M_g$	$Re$	g-r	Sérsic n	$EW(H\alpha)$
		(J2000)	(J2000)		$M_{\odot}$	(mag)	(kpc)			(Å)
(1)	(2)	(3)	(4)	(5)	(6)	(7)	(8)	(9)	(10)	(11)
The 33 AGN candidates using both spatially resolved and central $1''.5$ radius spectra										
7990–6102	1–24379	261.466028	56.852051	0.02679	9.44	-17.68	3.10	0.66	1.1	5.69
8081–3702 <sup>c</sup>	1–38166	49.946854	0.623822	0.02465	9.45	-18.58	2.23	0.37	3.4	2.64

manga-Plateifu	manga-ID	Ra (J2000)	Dec (J2000)	$z$	$\log M_{\star}$ $M_{\odot}$	$M_g$ (mag)	$Re$ (kpc)	g-r	Sérsic n	EW( $H\alpha$ ) (Å)
(1)	(2)	(3)	(4)	(5)	(6)	(7)	(8)	(9)	(10)	(11)
<sup>a</sup> 8084–1902 <sup>c</sup>	1–38618	52.622585	-0.488769	0.02173	9.67	-18.54	1.02	0.57	2.7	2.01
8155–1901	1–38510	53.023305	0.479390	0.02206	9.58	-18.41	1.60	0.57	1.6	2.78
8156–12704 <sup>c</sup>	1–205845	55.265549	-0.031234	0.03663	9.66	-18.79	5.15	0.57	1.0	1.29
8252–1902	1–138164	146.091838	47.459851	0.02590	9.40	-17.84	0.78	0.59	6.0	8.60
8258–1901	1–277213	166.620758	44.850902	0.02103	9.62	-18.57	1.28	0.52	0.9	29.61
8312–1901	1–210846	246.281956	39.435726	0.02962	9.68	-18.49	2.30	0.62	6.0	5.07
8320–3704	1–519742	206.612456	22.076742	0.02757	9.59	-18.82	2.68	0.60	1.3	13.12
8335–3703	1–252126	218.335552	40.550214	0.01816	9.41	-17.32	0.62	0.78	6.0	12.30
8338–9101	1–491095	171.966423	21.409205	0.02182	9.22	-17.96	3.22	0.38	0.9	4.41
8449–1902	1–488575	168.457073	22.810678	0.02237	9.52	-17.85	1.22	0.66	2.2	2.76
8483–1901	1–93551	246.311080	48.721331	0.02074	9.25	-17.25	0.61	0.64	6.0	3.42
8566–1901 <sup>c</sup>	1–338579	113.771912	41.974320	-0.00042	7.30	-12.13	0.00	0.86	6.0	0.69
8602–6101	1–211105	247.762350	39.623737	0.03242	9.60	-17.88	2.31	0.76	0.8	5.49
8613–1902	1–177127	255.290409	33.608349	0.03706	9.57	-18.97	1.40	0.44	1.3	33.92
<sup>a</sup> 8655–1902	1–29809	358.468819	-0.098731	0.02196	9.55	-18.15	1.37	0.64	1.8	2.75
<sup>a</sup> 8711–1901 <sup>c</sup>	1–379255	118.266565	52.743201	0.01846	9.48	-17.85	0.53	0.65	4.7	0.66
8711–1902	1–379008	118.761278	52.227437	0.02317	9.66	-18.34	1.27	0.66	2.0	9.34
8936–3704 <sup>c</sup>	1–152769	117.175199	30.171755	0.03587	9.64	-18.39	1.79	0.60	6.0	1.47
8937–1901	1–201307	116.997855	29.190689	0.02671	9.54	-18.21	1.62	0.57	3.3	15.74
<sup>a</sup> 8942–6101 <sup>c</sup>	1–230177	124.897858	26.362666	0.01999	9.60	-18.25	2.55	0.65	1.8	1.61
8982–3703	1–458092	203.190094	26.580376	0.04701	9.46	-18.93	1.24	0.43	2.4	87.01
8983–1901 <sup>c</sup>	1–457905	203.795827	25.946970	0.02594	9.42	-17.75	1.27	0.64	1.9	1.20
8992–1902	1–149501	173.721052	51.091462	0.02625	9.55	-18.05	1.94	0.62	1.5	2.81
8999–6104	1–148597	165.161806	50.201391	0.02317	9.66	-18.65	1.03	0.56	6.0	8.69
9002–3702	1–373057	222.190591	31.687042	0.03222	9.52	-17.75	1.86	0.76	1.9	4.80
9193–12703	1–109270	46.685858	-0.408800	0.02523	9.46	-18.28	1.46	0.51	0.9	9.02
9487–6102	1–45131	122.065499	45.284997	0.03979	9.55	-19.96	7.31	0.25	1.4	14.26
9505–3701 <sup>c</sup>	1–413676	139.139355	26.799501	0.02423	9.56	-17.99	2.23	0.62	2.1	1.68
9509–12701	1–298640	123.265370	24.566993	0.02049	9.65	-18.52	3.53	0.55	2.1	13.75
9872–1902	1–322575	233.815569	41.570527	0.02827	9.66	-18.24	1.12	0.67	1.1	4.92
10001–1901	1–55567	133.330028	57.041155	0.02575	9.45	-17.63	1.45	0.74	0.7	14.23
The 16 off-nuclear AGN candidates										
7960–9101	1–547621	259.206451	31.755753	0.02369	9.60	-18.86	3.54	0.47	1.3	7.68
8317–12705	1–259104	193.855953	43.938064	0.03873	9.62	-19.24	5.65	0.43	1.4	5.21
8335–12702	1–251764	215.487486	40.195802	0.01884	9.43	-18.53	3.96	0.39	1.6	4.49
8449–6104	1–488783	168.096446	23.169182	0.02291	9.55	-17.90	2.77	0.72	1.3	5.93

manga-Plateifu	manga-ID	Ra	Dec	$z$	$\log M_{\star}$	$M_g$	$Re$	g-r	Sérsic n	EW( $H\alpha$ )
		(J2000)	(J2000)		$M_{\odot}$	(mag)	(kpc)			(Å)
(1)	(2)	(3)	(4)	(5)	(6)	(7)	(8)	(9)	(10)	(11)
8464–6102	1–258752	186.000240	45.943987	0.02257	9.66	-19.02	2.84	0.43	0.8	6.36
8466–3702	1–277965	168.183562	45.187387	0.02336	9.45	-18.62	2.16	0.51	0.7	7.11
8485–12705	1–209111	235.410126	48.274017	0.03796	9.67	-19.01	4.16	0.50	1.4	8.96
8486–12704	1–209407	238.261763	46.767997	0.01951	9.39	-18.05	4.11	0.53	0.7	5.72
8623-9101	1–178698	311.347364	0.492529	0.01335	9.04	-18.03	2.19	0.47	1.6	10.05
8727–9102	1–51826	55.130622	-6.439925	0.02226	9.59	-19.08	3.29	0.35	0.7	24.46
8933–3704	1–457130	195.330499	27.860463	0.02741	9.43	-18.22	2.05	0.49	3.2	6.32
8941–12701	1–164062	120.063604	27.589989	0.02295	9.20	-18.45	4.24	0.36	1.2	5.53
8987–3704	1–386264	136.294847	28.285333	0.02709	9.61	-18.31	3.22	0.68	1.8	7.15
8997–1901	1–149624	171.357399	52.622878	0.02710	9.56	-18.31	1.77	0.53	1.1	4.54
9000–1902	1–149695	172.886300	52.656030	0.03382	9.56	-18.18	0.88	0.61	2.6	7.65
9501–1902	1–385052	129.634703	24.898774	0.02595	9.52	-17.91	1.39	0.63	1.1	4.83
The 11 AGN candidates using the spectra in the central 1".5 radius										
8335–12704	1–592984	215.718400	40.622597	0.01819	9.42	-17.76	3.86	0.54	1.2	3.98
8449–9101	1–488706	169.364330	23.346727	0.02232	9.27	-17.82	3.87	0.51	1.4	2.52
8601–6102	1–135512	247.711832	40.024799	0.02796	9.51	-17.89	3.44	0.57	2.8	3.59
8606–3704	1–136305	255.915543	36.384934	0.02467	9.52	-17.86	2.67	0.66	1.1	2.76
8612–9102	1–96154	254.397303	39.286089	0.03335	9.56	-18.34	2.92	0.57	1.0	4.12
8711–3703	1–379348	119.183464	52.989047	0.01784	9.05	-17.03	1.77	0.57	1.7	1.05
8941–9101	1–163975	120.203150	26.986272	0.02284	9.69	-18.35	3.50	0.64	3.8	0.88
8997–12703	1–149597	170.483361	52.850968	0.03370	9.63	-17.93	3.99	0.79	0.7	4.41
9486–3704	1–72128	122.052017	39.660395	0.01292	9.51	-17.94	1.23	0.64	1.1	1.24
9512–6103	1–53987	139.925621	1.325809	0.01650	9.37	-17.57	2.21	0.63	0.6	1.97
9868–12701	1–321290	218.468781	45.761149	0.03735	9.51	-18.34	3.53	0.85	1.5	3.39

### 2.1.2 Control Sample

To our purpose of exploring whether AGNs have affected the star formation of their host galaxies, we compare the stellar populations of AGN sample with those of control sample. The control galaxies are selected from the remaining 837 dwarf galaxies (not including the 60 AGN candidates). The first criterion we adopt to select control galaxies is

$$\Delta m = |\log M_{\star, \text{AGN}} - \log M_{\star, \text{ctr}}| \leq 0.1, \quad (1)$$

where  $M_{\star, \text{AGN}}$  and  $M_{\star, \text{ctr}}$  represent the stellar mass of a member galaxy in the AGN and control samples, respectively. The reason why we use the stellar mass as the primary criterion is that the physical properties (such as star formation rate, stellar age, and metallicity) of nearby galaxies are strongly correlated with their



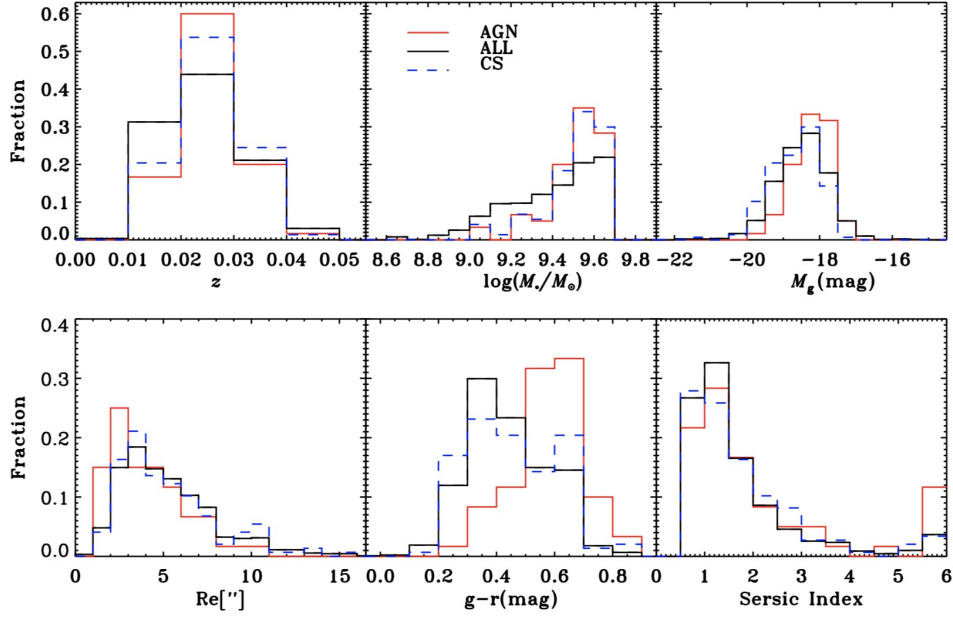


Fig. 3: The distributions of redshifts, stellar mass, absolute  $g$  band magnitude, effective radius, the  $g - r$  color and Sérsic index of the AGN sample (red), the control sample (blue) and the all dwarf galaxies (black). The  $g - r$  color of AGN sample is redder than that of the whole dwarf galaxies. All values are from the NSA catalog v1\_0.1 and assume  $h = 0.7$ . Magnitudes are K-corrected to rest-frame values and corrected for foreground Galactic extinction.

stellar masses (e.g., [Kauffmann et al. 2004](#); [Tremonti et al. 2004](#); [Wuyts et al. 2011](#); [Andrews & Martini 2013](#)).

For each AGN, there might be more than one normal dwarf galaxies meeting the above mass criteria, and thus for those matched sources we further limit its redshift ( $z$ ) to

$$\Delta z = \left| \frac{z_{\text{AGN}} - z_{\text{ctr}}}{z_{\text{AGN}}} \right| \leq 0.1. \quad (2)$$

We have then selected three control galaxies with the closest match in stellar mass for each AGN. Different AGNs are allowed to share the same control galaxy. For two AGN candidates (8982-3703 and 9486-3704) we have to adopt  $\Delta z \leq 0.2$  to select 3 control galaxies, and for one AGN candidate (8566-1901) we find no control galaxies.

We further check if the galactic properties of the control sample are indeed compatible with those of the AGN sample. As shown in Figure 3, we show the distributions of redshifts, stellar mass, absolute  $g$  band magnitude, effective radius, the  $g - r$  color and Sérsic index for the two samples. We can find that the distributions of the galactic properties are almost similar except for the  $g - r$  color. The median values of the  $g - r$  color for the AGN and control samples are 0.58 and 0.44, respectively. We will further discuss the effects of the different  $g - r$  color in Section 4.1.

## 2.2 Spectra Stacking

MaNGA provides spatially resolved spectra for every target galaxy, while the spectra of outer regions have low S/N (especially for these dwarf galaxies), which could cause large uncertainty in deriving the SFHs. [Cid Fernandes et al. \(2005\)](#) have found that the derived mean stellar ages ( $\langle \log t_{\star} \rangle_M$  and  $\langle \log t_{\star} \rangle_L$ , see Section 3) depend on the S/N of the input spectra with the rms less than 0.1 dex for  $S/N > 10$ .

In order to increase the S/N, we have used elliptical annuli to radially bin the datacube of each galaxy, as shown in [Figure 1](#). The width of the elliptical annuli is determined by the  $Re$  (NSA\_ELPETRO\_TH50\_R) and the S/N (=mean/rms flux) measured in the relatively clean window between 4730 and 4780Å. Each pixel size is  $0''.5$ , therefore, the annular width we set is equal to  $(0.5/Re+0.01) Re$ , which ensure that the minimum width is larger than  $0''.5$ . The width is increased until the binned spectrum has a  $S/N \geq 10$ . We note that for some sources the central spaxel has a  $S/N > 10$ , whereas the most outer region can not reach  $S/N > 10$ . During the binning process, we visually checked the contamination from foreground stars and/or neighbor galaxies, and masked those spaxels which could severely affect the binned spectra. However, we do not remove those spaxels located within the most outer region since the binned spectra generally have  $S/N < 10$  (see the green elliptical annuli in [Figure 1](#)) and are not included in our analysis.

## 2.3 Stellar Population Synthesis

In order to derive the stellar populations of each binned spectrum for these dwarf galaxies, we employ the stellar population synthesis code, STARLIGHT ([Cid Fernandes et al. 2005](#), hereafter C05; [Mateus et al. 2006](#); [Asari et al. 2007](#)). This code searches the best match between the observed spectra and the model spectra by linearly combining  $N_{\star}$  simple stellar populations (SSPs), which were published by [Bruzual & Charlot \(2003\)](#) using the evolutionary synthesis models with the [Salpeter \(1955\)](#) initial mass function, Padova-1994 models, and the STELIB library ([Le Borgne et al. 2003](#)). In this work, the model library comprises  $N_{\star} = 100$  SSPs which span 25 ages (from 1 Myr to 18 Gyr) and 4 metallicities ( $Z=0.005, 0.02, 0.2, \text{ and } 0.4Z_{\odot}$ ), following [Zhao et al. \(2011\)](#) and [Cai et al. \(2020\)](#). The SSPs are normalized at an arbitrary  $\lambda_0$  wavelength, reddened by a intrinsic extinction ( $A_{V,\star}$ ) assuming a foreground screen dust geometry with [Calzetti et al. \(1994\)](#) extinction law where  $R_V = 4.05$  ([Calzetti et al. 2000](#)) and weighted by the population vector  $\mathbf{x}$  which represents the fractional contribution of each SSP to the total synthetic flux at the normalized  $\lambda_0$ .

Prior to the fitting, the Galactic extinction law of [Cardelli et al. \(1989\)](#) and [O'Donnell \(1994\)](#) with  $R_V = 3.1$  is adopted to correct the observed spectra for Galactic extinction with the  $A_V$  values from [Schlegel et al. \(1998\)](#) as listed in the NASA/IPAC Extragalactic Database (NED). Meanwhile, the observed spectra are corrected for redshift and are rebinned to  $1\text{\AA}$  sampling with Cubic Spline Interpolation. The normalization wavelength we adopted is  $\lambda_0=4020\text{\AA}$  and the S/N of the observed spectra is calculated in the range free of emission lines between 4730 and 4780Å. The region of the spectra used to fit is from 3800 to 8900Å with masks of 20-30Å around the obvious emission lines, and the fitted regions are weighted equally, except for the stellar absorption features (e.g., CaIIK $\lambda$ 3934; CaII triplets), which are the strongest and less affected by nearby emission lines. More detailed informations about the synthesis process are presented in C05, [Mateus et al. \(2006\)](#) and [Zhao et al. \(2011\)](#).

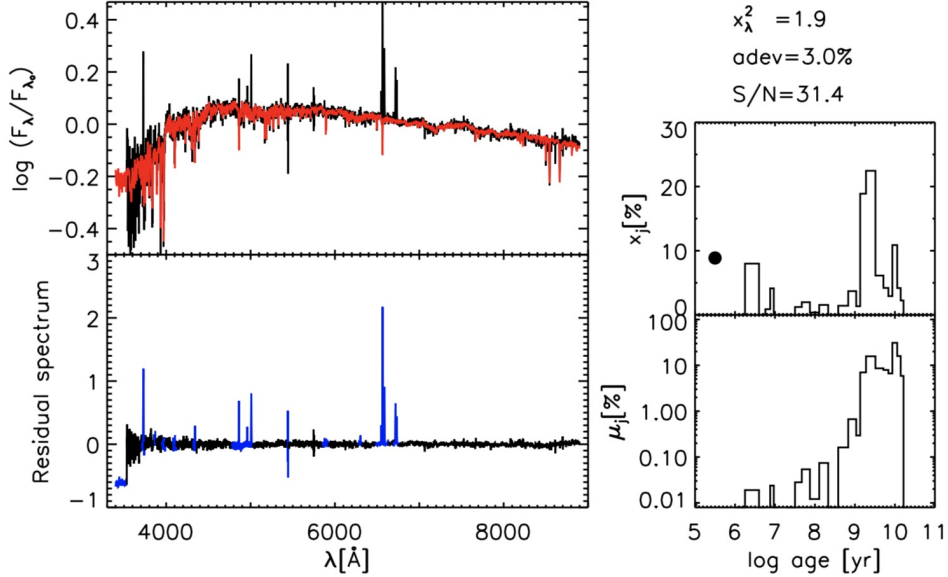


Fig. 4: Results of the spectral fitting for the stacked spectrum (0.01–0.21 Re) of 9193-12703. The logarithm of the observed (black) and the synthetic (red) spectra are shown in the top left panel and the spectra are normalized to  $\lambda_0 \sim 4020\text{\AA}$ . The bottom left panel displays the residual spectrum and the masked regions are replotted with a blue line. The right panels show the population vector binned in the 25 ages of SSPs used in the model library. The flux fraction vector and mass fraction vector are shown in top panel and bottom panel, respectively. The power-law component  $x_{\text{AGN}}$  is plotted with an (arbitrary) age of  $10^{5.5}$  yr and marked by a black point.

In addition, it is essential to add a non-stellar component (function of the form  $F_\nu \propto \nu^{-1.5}$ ) during the fitting process to represent the contribution of an AGN featureless continuum to the stellar base for the AGN sample, as same as previous works (e.g., C04; Koski 1978; Riffel et al. 2009). As pointed out in C04, the STARLIGHT code is incapable of discriminating between a  $F_\nu \propto \nu^{-1.5}$  power-law continuum and the spectrum of a dusty starburst, which could cause an overestimation of the mean stellar age. We re-ran the code without adding an AGN featureless continuum for all binned spectra and compared the returned stellar ages with those with an AGN featureless continuum. The stellar ages do not change much except for the binned spectra in five galaxies, while this does not affect our conclusion. We also investigated the fitted  $A_V$  as in Cai et al. (2020) to avoid any unreasonable results. We re-ran the code by setting the lower limit of  $A_V = 0$  for about 100 binned spectra with their fitted  $A_V < 0$ , among which about 40% sources have their  $A_V < -0.1$ . The re-fitted results have no significant change when the  $A_V$  is close to zero, and the re-fitted results are adopted for these binned spectra. In Figure 4, we show a typical example of our fitting results for the stacked spectrum of 9193-12703.

### 3 RESULTS AND ANALYSIS

According to the fractional contribution of flux and mass from different SSPs returned by STARLIGHT, we could calculate the mean stellar age, mean stellar metallicity, which are the most important stellar population parameters. We calculate the light- and mass-weighted mean stellar ages using the equations described in C05, i.e.

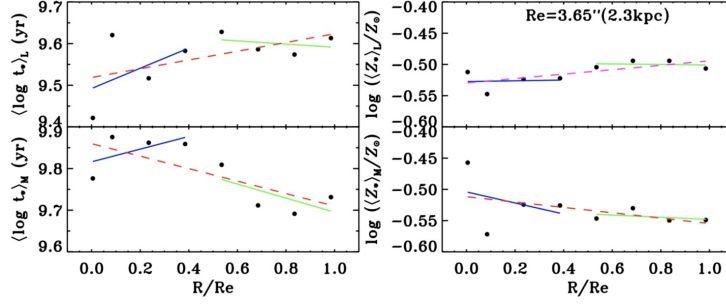


Fig. 5: A linear fitting example for MaNGA source 8312-1901. The left two panels show the linear fitting of the light-weighted mean stellar age (upper) and mass-weighted mean stellar age (bottom). The right two panels show the linear fitting of the light-weighted mean metallicity (upper) and mass-weighted mean metallicity (bottom). In each panel, The blue, green and red lines are the linear fit in  $0 - 0.5R_e$ ,  $0.5 - 1R_e$  and  $0 - 1R_e$ , respectively.

$$\langle \log t_* \rangle_L = \sum_{j=1}^{N_*} x_j \log t_j, \quad (3)$$

for the light-weighted mean stellar age, and

$$\langle \log t_* \rangle_M = \sum_{j=1}^{N_*} \mu_j \log t_j, \quad (4)$$

for the mass-weighted mean stellar age. Here  $t_j$  is the age value of the  $j$ th base,  $N_*$  is the total number of SSPs, and  $x_j(\mu_j)$  represent the light (mass) fraction of the  $j$ th base. As described in C05 and Zhao et al. (2011),  $\langle t_* \rangle_L$  is associated with the recent SFH, while  $\langle t_* \rangle_M$  mainly depend on the mass assembly history.

Similarly, we calculate the light- and mass-weighted mean metallicity using

$$\langle Z_* \rangle_L = \sum_{j=1}^{N_*} x_j Z_j, \quad (5)$$

and

$$\langle Z_* \rangle_M = \sum_{j=1}^{N_*} \mu_j Z_j, \quad (6)$$

where  $Z_j$  is the metallicity value of the  $j$ th base.

According to the spatially resolved mean stellar age and mean stellar metallicity, we get the radial age and metallicity profiles for each AGN-host dwarfs. The low-level active galaxies should have effects on the stellar populations in the nuclear regions. The IFU of all MaNGA galaxies are covered to at least  $1.5 R_e$ , however, the radial profiles could not reach  $1.5 R_e$  due to poor S/N for the dwarf galaxies. Some previous works (e.g., Mallmann et al. 2018) have adopted  $0.5 R_e$  as the division to make comparison between active galaxies and no-active galaxies. Therefore, we measure the gradients of the profiles of individual galaxies in  $0-0.5 R_e$ ,  $0.5-1 R_e$ , and  $0-1 R_e$ , respectively. We adopt a straight line to fit the data points with the following equation

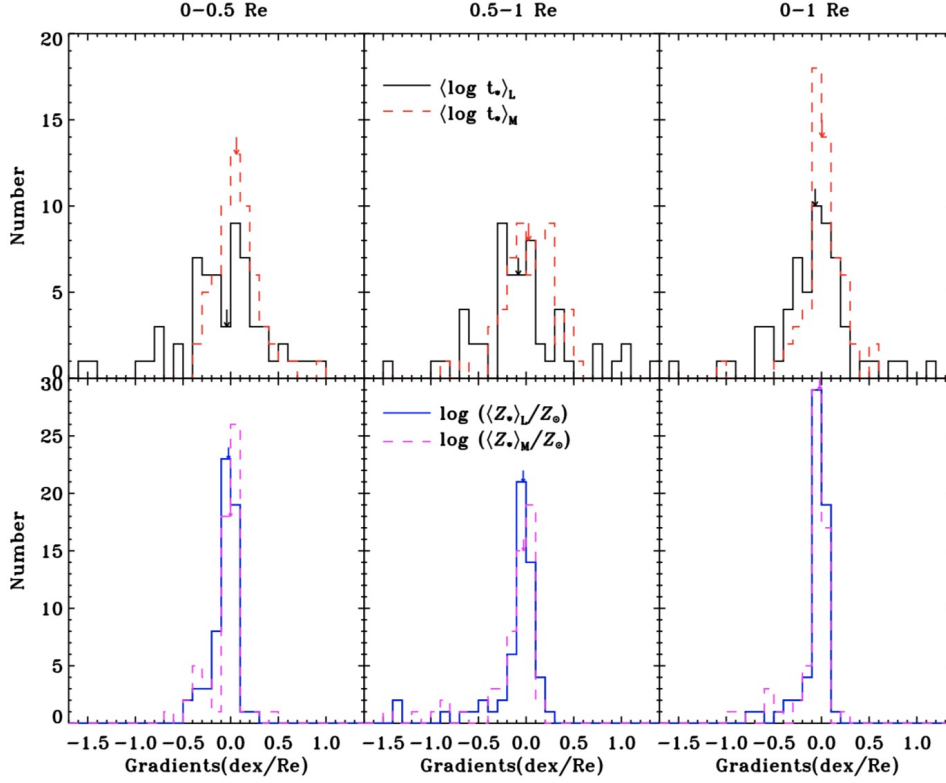


Fig. 6: Number distributions of the gradients of the stellar age (upper) and stellar metallicity (bottom). The left, middle and right panels show the distributions of the gradients in  $0-0.5 Re$ ,  $0.5-1 Re$  and  $0-1 Re$ , respectively. Arrows in each panel represent the median values of gradients.

$$y = y_o + \nabla \times x, \quad (7)$$

where  $y = \langle \log t_* \rangle$  ( $\log \langle (Z_*) / Z_\odot \rangle$ ), the stellar age (metallicity),  $x = r/Re$ , the normalized radius, and  $\nabla = \nabla_t$  ( $\nabla_Z$ ), the gradient of stellar age (metallicity) in units of dex/Re. In Figure 5, we take MaNGA source 8312-1901 as an example to show our fitting.

Based on the fractional contribution of each SSP, we can reconstruct the SFHs. However, as discussed in C05, the individual components of  $x$  returned by STARLIGHT have large uncertainties. Therefore, we adopt the same method with previous work (e.g., C05, Zhao et al. 2011, Cai et al. 2020), which binning vectors of  $x$  into three components, i.e. the young ( $t < 10^8$  yr), intermediate ( $10^8 < t < 10^9$  yr), and old ( $t > 10^9$  yr) populations. The uncertainties of these three components are less than 0.05, 0.1, and 0.1, respectively, for  $S/N > 10$ . For each binned spectrum of the dwarf galaxies, the individual components  $x$  are binned into these three components ( $x_Y$ ,  $x_I$  and  $x_O$ ), respectively. In order to measure the gradients of the  $x_Y$  ( $\nabla_{x_Y}$ ), we further adopt a straight line to fit the  $x_Y$  for each AGN and control galaxy in  $0-0.5 Re$ ,  $0.5-1 Re$ , and  $0-1 Re$ .

### 3.1 Radial stellar age

In the upper panel of Figure 6, we show the distributions of  $\nabla_t$  for the AGN sample. The AGN sample has a wide and similar distribution in  $\nabla_{t_L}$  ( $\nabla_{t_M}$ ), ranging from  $\sim -1.6$  ( $-0.5$ ) to  $\sim 1.0$  ( $1.0$ ) in  $0-0.5 Re$ ,  $\sim -1.5$  ( $-$

1.0) to  $\sim 1.1(0.5)$  in  $0.5-1 Re$  and  $\sim -1.6(-1.0)$  to  $\sim 1.2(0.6)$  in  $0-1 Re$ . The median values of  $\nabla_{t_L}(\nabla_{t_M})$  are  $-0.04 \pm 0.36^3$  ( $0.06 \pm 0.21$ ) in  $0-0.5 Re$ ,  $-0.08 \pm 0.30$  ( $0.03 \pm 0.26$ ) in  $0.5-1 Re$  and  $-0.07 \pm 0.26$  ( $0.00 \pm 0.14$ ) in  $0-1 Re$ , respectively. The gradients of individual galaxies in different regions are different. However, the median values of the gradients are all close to 0 and this suggests that the overall behavior of the  $\langle \log t_* \rangle_L$  profiles for these AGN-host dwarfs are almost flat. We will further show the co-added radial stellar age in next section.

Regarding the radial metallicity profiles, the gradients of the individual source are also diverse. However, the profiles tend to be flat or negative with few sources having the gradients greater than 0.2. Meanwhile, the median values of  $\nabla_{Z_L}(\nabla_{Z_M})$  are  $-0.02 \pm 0.07$  ( $0.00 \pm 0.04$ ) in  $0-0.5 Re$ ,  $-0.03 \pm 0.09$  ( $-0.03 \pm 0.09$ ) in  $0.5-1 Re$  and  $-0.02 \pm 0.05$  ( $-0.02 \pm 0.04$ ) in  $0-1 Re$ . Therefore, the metallicity profiles tend to be negative but close to zero. We will further discuss the overall behavior of the stellar metallicity in next section.

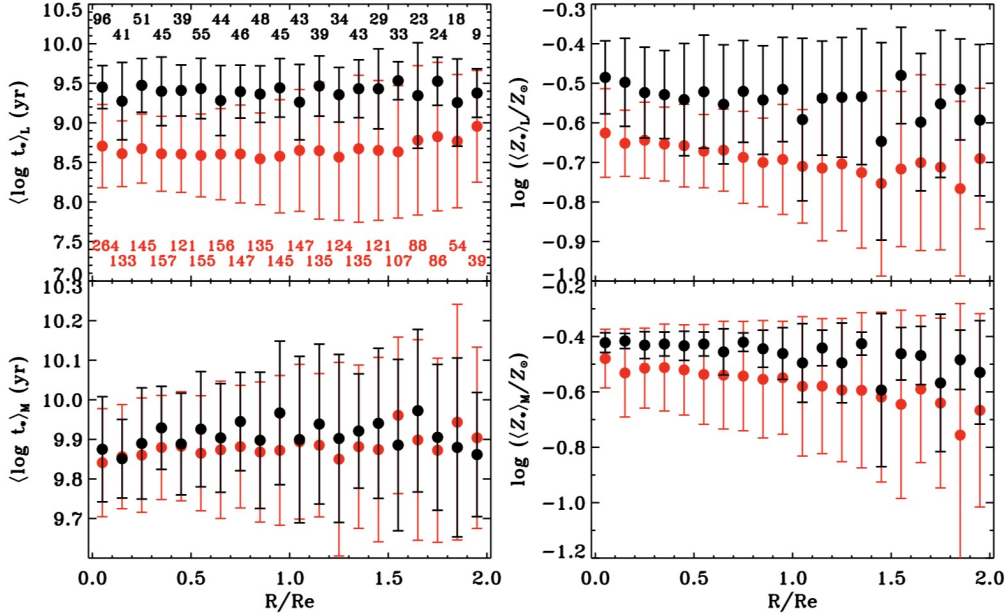


Fig. 7: Co-added stellar age and metallicity profiles for the AGN and control samples. The left two panels show the co-added light- and mass-weighted mean stellar age profiles. The right two panels show co-added light- and mass-weighted metallicity profiles. The dots with error bars show the median value and  $1\sigma$  dispersion. The co-added radial profiles for the AGN and control samples are shown with black and red colors, respectively. In the upper left panel, numbers of data points in each bin are labeled with black and red colors for the AGN and control samples, respectively.

### 3.2 Co-added radial properties

In order to investigate AGN effects on host galaxies, we further compare the overall behavior of the stellar age and metallicity by plotting the co-added radial profiles for the AGN and control samples, as shown in Figure 7. Since we select 3 control galaxies for each AGN, and different AGNs are allowed to share the same control galaxy. Therefore we remove the repeated control galaxies and the control sample finally

<sup>3</sup> Throughout the paper, the uncertainty of a median value is estimated using  $1.48 \times \text{MAD}$  assuming normally distributed noise, where MAD is the median value of the absolute deviations from the median data.

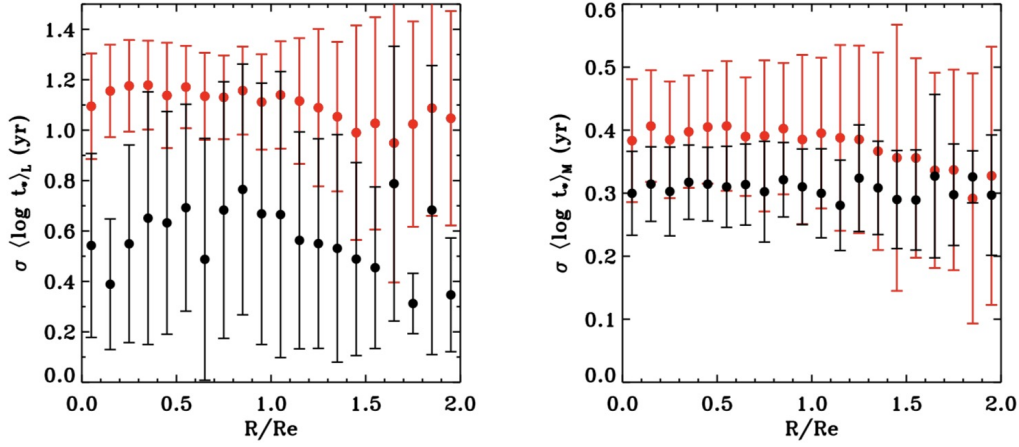


Fig. 8: Co-added standard deviations of the log age profiles for the AGN and control samples. The dots with error bars show the median value and  $1\sigma$  dispersion. The co-added radial profiles for the AGN and control samples are shown with black and red colors, respectively.

Table 2: The gradients of the stellar age and stellar metallicity

	AGN		AGN (EW(H $\alpha$ ) > 3Å)		Control	
	inner (0–1 Re)	outer (1–2 Re)	inner (0–1 Re)	outer (1–2 Re)	inner (0–1 Re)	outer (1–2 Re)
$\langle \log t_{\star} \rangle_L$	-0.01	0.02	-0.05	-0.03	-0.12	0.31
$\langle \log t_{\star} \rangle_M$	0.08	-0.04	0.09	-0.03	0.03	0.05
$\log(\langle Z_{\star} \rangle_L / Z_{\odot})$	-0.04	0.00	-0.03	0.03	-0.07	-0.01
$\log(\langle Z_{\star} \rangle_M / Z_{\odot})$	-0.03	-0.06	-0.03	-0.05	-0.06	-0.13

includes 147 individual dwarf galaxies. We radially bin the stellar age and metallicity with width of 0.1 effective radius ( $Re$ ) for the two samples. Due to the few data points in 1-2  $Re$  for the individual galaxy, we do not measure the gradients in 1-2  $Re$ . However, the co-added radial profiles can reach the radius of  $\sim 2 Re$ , which can be used to explore the properties in the outer region, and thus we measure the gradients in the inner (0–1  $Re$ ) and outer (1–2  $Re$ ) regions.

As shown in the bottom left panel of Figure 7, the median values of  $\langle \log t_{\star} \rangle_M$  are both about 9.8–10.0 within 2  $Re$  for the two samples. Meanwhile, the  $1\sigma$  dispersions of the  $\langle \log t_{\star} \rangle_M$  shown by error bars range from  $\sim 0.1$  dex to  $\sim 0.3$  dex. Therefore, for these dwarf galaxies, the stellar mass is mainly contributed by the old population, which is similar to previous works (e.g., Zhao et al. 2011; Cai et al. 2020).  $\nabla_{t_M}$  in the inner and outer regions are shown in Table 2. For both samples,  $\nabla_{t_M}$  are close to 0 in the inner and outer regions, which suggest that the  $\langle \log t_{\star} \rangle_M$  profiles are generally flat. This is a natural result, as the present stellar mass is mainly contributed by old population for these objects.

Regarding  $\langle \log t_{\star} \rangle_L$ , the gradients for the control sample are -0.12 and 0.31 in the inner and outer regions, respectively. The  $\langle \log t_{\star} \rangle_L$  profile of the control sample show a ‘U’ shape curve with the minimum value located around 1–1.5  $Re$ . A series of works (e.g., Zheng et al. 2015; Ruiz-Lara et al. 2016; Zheng et al. 2017) have found that the  $\langle \log t_{\star} \rangle_L$  profiles of disk galaxies show a ‘U’ shape with the minimum value located around 1–1.5  $Re$ . This may be caused by the stellar radial migration as suggested in numerical

simulations (e.g., [Sellwood & Binney 2002](#); [Roškar et al. 2008](#)). However, the gradients for the AGN sample are almost zero in the inner and outer regions, as shown in Table 2. One possible explanation might be that the AGN-host dwarf galaxies are almost quiescent due to the AGN effects which resulting in an overall quenching of the dwarf galaxies.

The median values of  $\langle \log t_{\star} \rangle_L$  for the AGN sample are in the range of 9.3–9.5, which indicate that these AGN-host dwarfs are almost quiescent in the last 2–3 Gyr within  $2 R_e$ . The  $\langle \log t_{\star} \rangle_L$  profile for the AGN sample removing the 16 off-nuclear AGN candidates has no significant change. For the control sample, the median values of  $\langle \log t_{\star} \rangle_L$  range from  $\sim 8.5$  to  $\sim 8.9$  within  $2 R_e$ , which are significantly smaller than those for the AGN sample, with differences ranging from  $\sim 0.4$  dex to  $\sim 0.9$  dex. It can be found that the  $\langle \log t_{\star} \rangle_L$  of the AGN sample are very old and significantly older than the control sample selected with stellar mass as main criterion. This indicates that these AGN-host dwarfs almost keep quiescent within  $2 R_e$ . The reason for the weaker star formation in these AGN-host dwarf galaxies might be the lack of the gas. Some works (e.g., [Bradford et al. 2018](#); [Sharma et al. 2020](#)) have found evidences of reduced HI gas mass in isolated AGN-host dwarf galaxies, indicating a high degree of cold gas depletion. The relatively older stellar ages of AGN host dwarfs imply that AGNs might accelerate the evolution of galaxies by accelerating the consumption of the cold gas, resulting in an overall quenching of the dwarf galaxies.

However, some works (e.g., [Storchi-Bergmann et al. 2001](#); [Rembold et al. 2017](#)) have found that the AGN activities in massive galaxies might be related to recent episodes of star formation in the nuclear region. [Cai et al. \(2020\)](#) also found not all AGN-host dwarf galaxies are old. Out of the 136 AGN-host dwarf galaxies, 15 galaxies (11%) have  $\langle \log t_{\star} \rangle_L < 8$  and 68 (50%) galaxies have  $8 < \langle \log t_{\star} \rangle_L < 9$ . Further, a mild correlation is found between the SFHs and  $L_{[\text{O III}]}$ , for sources with  $L_{[\text{O III}]} > 10^{39} \text{ erg s}^{-1}$ . An possible explanation is that these AGN-host dwarfs stand in different stages of evolution. At the early time when the host galaxies have abundant cold gas which can fuel the AGN and be used to star formation, we observe a young stellar age in at least the central region. The AGN-host dwarfs with old stellar age are in the late stages of evolution, in which the host galaxies almost have no recent star formation due to the lack of cold gas. Meanwhile, as shown in Section 3.4, most of our AGN-host dwarf galaxies are low-level AGNs, with only eight sources having  $L_{[\text{O III}]} > 10^{39.5} \text{ erg s}^{-1}$ . The weak strength of these AGNs might be also due to the lack of gas, which is consistent with our previous explanation.

Therefore, an entire picture might be that the stellar age of AGN-host dwarfs is young and the AGNs tend to be strong when the cold gas of host galaxies are abundant, which can feed black holes and be used for star formation. As the fast consumption of cold gas by BHs or even AGN feedback, the dwarf galaxies gradually quench due to the lack of cold gas, and the AGNs also become weak. Further, the quenched dwarf galaxies are likely the low-mass analogues of the 'red geysers' suggested by ([Cheung et al. 2016](#)), which keep quiescent as the low-level AGNs suppress the star formation by hampering the cooling of the gas ([Penny et al. 2018](#)).

The  $1 \sigma$  dispersion represents the diversity of the mean stellar age in the dwarf galaxies. Since the  $\langle \log t_{\star} \rangle_L$  of most AGN-host dwarfs are old within  $2 R_e$ , the  $1 \sigma$  dispersions of  $\langle \log t_{\star} \rangle_L$  ( $\sim 0.2$ – $\sim 0.6$  dex) for the AGN sample are smaller than those ( $\sim 0.4$ – $\sim 0.9$  dex) for the control sample. The  $1 \sigma$  dispersions of  $\langle \log t_{\star} \rangle_L$  become larger with increasing  $R_e$ , especially for the control sample, which might be caused



by the less data points in high  $Re$ . We further find that the  $1\sigma$  dispersions of the control sample (0.4–0.9 dex) are larger than those of the low-mass sample ( $\sim 0.5$  dex) in Zheng et al. (2017). This is caused by the different methods used to calculate the stellar age. As described in Section 3, this work use the  $\log t_j$  before weighting, which may give more weight to younger stellar populations. For the control sample, we also calculate the  $\langle \log t_\star \rangle_L$  by adopting the same definitions with Zheng et al. (2017), and the  $1\sigma$  dispersions of  $\langle \log t_\star \rangle_L$  significantly decrease, ranging from  $\sim 0.2$  dex to  $\sim 0.5$  dex.

In the right panel of Figure 7, we display the metallicity profiles for both samples. As shown in Table 2,  $\nabla_{Z_L}$  for the AGN (control) sample are -0.04 (-0.07) in the inner region and 0.0 (-0.01) in the outer region. Meanwhile,  $\nabla_{Z_M}$  for the AGN (control) sample are -0.03 (-0.06) in the inner region and -0.06 (-0.13) in the outer region. The gradients of mean stellar metallicity are close to 0 but slightly negative, which suggest that the metallicity profiles have a decreasing trend with increasing radius. This is consistent with the results of other works (e.g., Morelli et al. 2015; Zheng et al. 2017), and the similar metallicity profiles for the AGN and control samples suggest that AGNs unlikely have a strong impact on the chemical evolution of the host galaxy, which corresponds with the results of Cai et al. (2020).

According to C05, we can further investigate the SFH by analyzing the light- and mass-weighted standard deviations of the log age, which are useful to identify whether galaxies are dominated by a single population or have bursty or continuous SFHs. The definitions of these two parameters are

$$\sigma_L(\log t_\star) = \left[ \sum_{j=1}^{N_\star} x_j (\log t_j - \langle \log t_\star \rangle_L)^2 \right]^{1/2} \quad (8)$$

and

$$\sigma_M(\log t_\star) = \left[ \sum_{j=1}^{N_\star} \mu_j (\log t_j - \langle \log t_\star \rangle_M)^2 \right]^{1/2}. \quad (9)$$

In Figure 8, we plot the radial median values of  $\sigma_L(\log t_\star)$  and  $\sigma_M(\log t_\star)$  for the AGN and control samples. It can be found that these dwarf galaxies are not dominated by a single population, as the median values of the  $\sigma_L(\log t_\star)$  and  $\sigma_M(\log t_\star)$  within  $2Re$  are greater than zero. The median values of  $\sigma_L(\log t_\star)$  tend to be larger than  $\sigma_M(\log t_\star)$ . This indicates that the mass assembly history of these dwarf galaxies is relatively narrow, while repeated/continuous star formation activities might exist during the lifetime of dwarf galaxies. Further, there exist differences in the median values of  $\sigma_L(\log t_\star)$  between the AGN and control sample: the median values of  $\sigma_L(\log t_\star)$  within  $2Re$  range from 0.3 (1.0) to 0.8 (1.2) for the AGN (control) sample. This is a reasonable result, as the AGN sample is dominated by old stellar populations.

### 3.3 Dependence on the Host Galaxy Morphology

The SFHs of galaxies are related to the galaxy morphology. A series of works have studied the relationship between the nuclear stellar population and the AGN host galaxy morphology. Most of works found no correlation between the nuclear star formation and the host galaxy morphology (e.g., C04; Cai et al. 2020). Mallmann et al. (2018) further tried to study the spatially resolved stellar population of AGN host galaxies

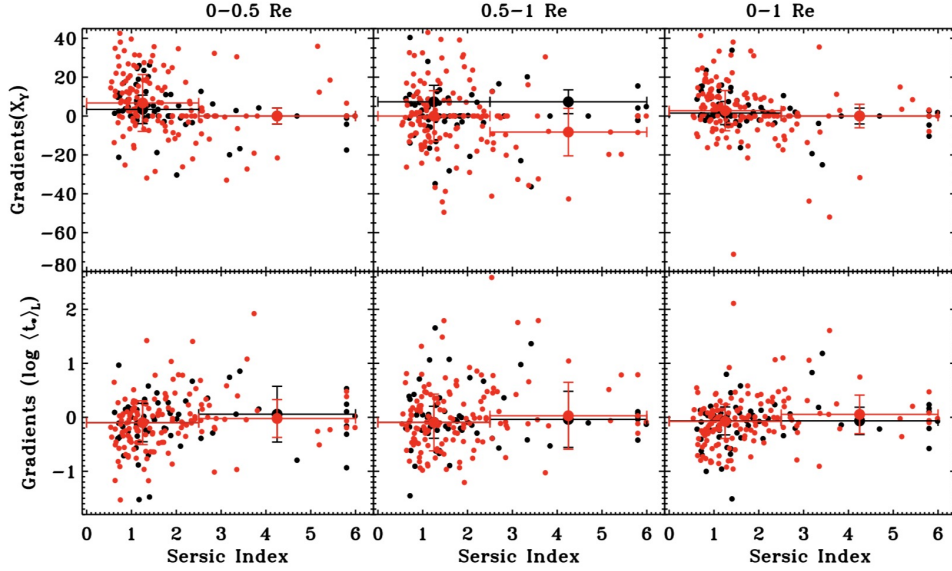


Fig. 9: Plot of Sérsic index  $n$  of the dwarf galaxies versus  $\nabla_{x_Y}$  (upper) and  $\nabla_{t_L}$  (bottom) in  $0-0.5 Re$ ,  $0.5-1 Re$  and  $0-1 Re$ , respectively. In each panel, the AGN and control samples are represented with the black and red circles, respectively. The bigger black (red) solid circles represent the median values of the gradients for early-type ( $n > 2.5$ ) and late-type ( $n < 2.5$ ) AGN-host dwarf (control) galaxies, with error bars in the  $y$ -axis giving the dispersion of the data within each bin.

and found no significant differences between early- and late-type host galaxies. In this paper, for these AGN-host dwarf galaxies, we try to search the correlation between the gradients of SFHs and the host galaxy morphology.

Since the detailed Hubble morphology of dwarf galaxies are not easy to recognized, we use the Sérsic index as galaxy morphology parameter. By adopting  $n = 2.5$  as the dividing line (e.g., Barden et al. 2005), the dwarf galaxies were classified as early- ( $n > 2.5$ ) and late-type ( $n < 2.5$ ) galaxies. As shown in Figure 9, we plot the Sérsic index  $n$  against  $\nabla_{t_L}$  and  $\nabla_{x_Y}$  with the median values of gradients overlaid. From the figure we can find that, for both the AGN and control samples, the  $\nabla_{t_L}$  and  $\nabla_{x_Y}$  in  $0-0.5 Re$ ,  $0.5-1 Re$  and  $0-1 Re$  almost have no correlation with  $n$ . Furthermore, we can find that the median values of  $\nabla_{t_L}$  and  $\nabla_{x_Y}$  almost have no differences between the AGN sample and the control sample except for the  $\nabla_{x_Y}$  in  $0.5-1 Re$ . However, the median values of of the  $\nabla_{x_Y}$  in  $0.5-1 Re$  for both samples are similar when we consider the errors. Therefore, for both samples, no obvious correlations between the gradients of SFHs within  $1 Re$  and the morphology are found.

### 3.4 [O III] Luminosity of the AGN sample

As discussed in Section 3.2, most of AGN candidates keep quiescent due to the lack of gas, which suggest that the strength of these AGNs should be weak. Here we research the [O III] luminosity of these AGN candidates, as Kauffmann et al. (2003) have shown that the [O III]  $\lambda 5007$  line luminosity,  $L_{[\text{O III}]}$ , is a good tracer of AGN activity (see also Trump et al. 2015). We derive the [O III] luminosity for these AGN candidates by using the central  $1''.5$  radius spectra, and the  $L_{[\text{O III}]}$  are corrected for extinctions, which are measured from the observed  $H\alpha/H\beta$  Balmer decrement (see section 3.7 of Cai et al. 2020).

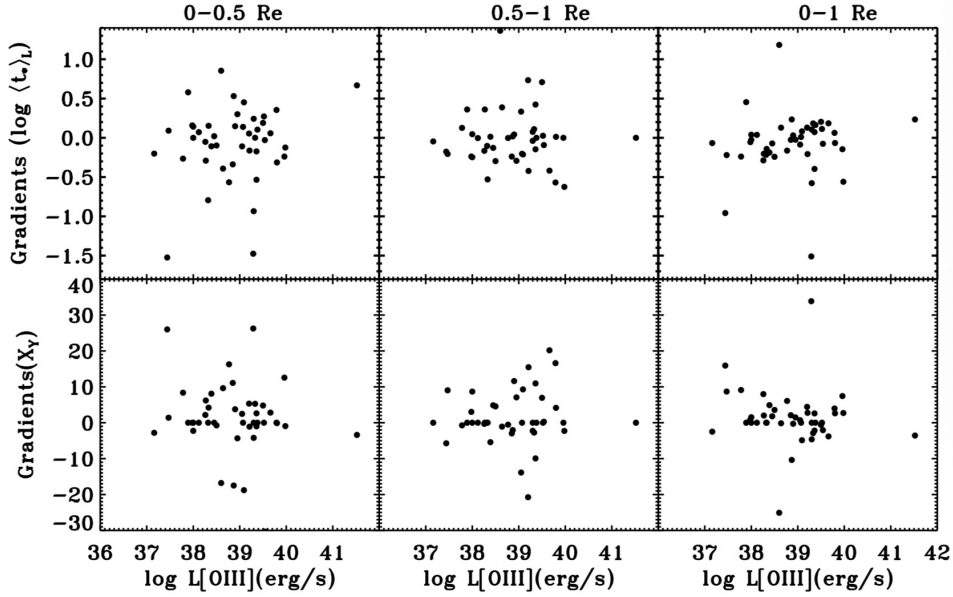


Fig. 10: Plot of the [O III]  $\lambda 5007$  luminosity versus  $\nabla_{t_L}$  (upper) and  $\nabla_{x_Y}$  (bottom) in  $0-0.5 Re$ ,  $0.5-1 Re$  and  $0-1 Re$ , respectively.

As shown in Figure 10, out of 44 AGN candidates classified as AGNs using the spectra from the central  $1''.5$  radius, the  $L_{[\text{O III}]}$  of 36 objects is in the range of  $10^{36.5} - 10^{39.5} \text{ erg s}^{-1}$  (i.e.  $10^3 - 10^6 L_{\odot}$ ), and only one object can be characterized as “strong AGN”, as its  $L_{[\text{O III}]} \geq 10^7 L_{\odot}$  (e.g., Kauffmann et al. 2003). This confirms that the AGN candidates are the low-level AGNs. Cai et al. (2020) have found a mild (anti-) correlation between  $x_Y$  ( $\langle \log t_{\star} \rangle_L$ ) and  $L_{[\text{O III}]}$ , for sources with  $L_{[\text{O III}]} > 10^{39} \text{ erg s}^{-1}$ . Based on their work, the stellar populations of nuclear regions tend to be younger when AGN becomes stronger. This indicates that a positive (negative) correlation might be found between  $\nabla_{t_L}$  ( $\nabla_{x_Y}$ ) in the inner region and  $L_{[\text{O III}]}$ . As shown in Figure 10, no obvious correlation is found between  $\nabla_{t_L}$  ( $\nabla_{x_Y}$ ) and  $L_{[\text{O III}]}$ . The Spearman correlation coefficients ( $\rho$ ) are 0.09(-0.15), -0.02(0.15) and 0.23(-0.20) in  $0-0.5 Re$ ,  $0.5-1 Re$  and  $0-1 Re$ , respectively, with  $p$ -values of  $5.8 \times 10^{-1}$  ( $3.3 \times 10^{-1}$ ),  $8.9 \times 10^{-1}$  ( $3.2 \times 10^{-1}$ ) and  $1.2 \times 10^{-1}$  ( $1.9 \times 10^{-1}$ ). Most of the AGN candidates are low-level AGNs, therefore, no correlation between the gradients and  $L_{[\text{O III}]}$  might be due to few strong sources.

## 4 DISCUSSION

### 4.1 The selection effect of the AGN sample

As shown in Figure 3, the median values of the  $g - r$  color for the AGN and control samples are 0.58 and 0.44, respectively. The redder color of this AGN sample is likely caused by a selection effect, which might miss the young AGN dwarf galaxies by BPT diagram due to the AGN radiation being severely contaminated by the strong radiation from HII regions. Therefore, it is essential to consider the effect of the different  $g - r$  color when we compare the stellar ages between the AGN and control samples.

Fortunately, Zhao et al. (2011) have suggested that the fitted  $\langle \log t_{\star} \rangle_L$  has a good correlation with the  $g - r$  color. Based on their work (see Figure 9 in Zhao et al. 2011), the AGN sample is 0.14 mag (median) redder than the control sample in  $g - r$  color, which causes that the  $\langle \log t_{\star} \rangle_L$  of the AGN sample is about

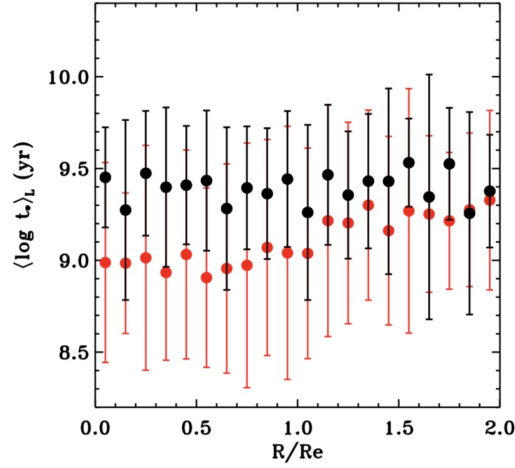


Fig. 11: Co-added stellar age profiles for the AGN and new color-selected control samples. The dots with error bars show the median value and  $1\sigma$  dispersion. The co-added radial profiles for the AGN and control samples are shown with black and red color, respectively.

0.3–0.4 dex older than that of control sample. However, as shown in Figure 7, the differences between the two samples in  $\langle \log t_{\star} \rangle_L$  range from  $\sim 0.4$  dex to  $\sim 0.9$  dex within the  $2 R_e$ . The AGN sample is still  $\sim 0.3$ – $\sim 0.6$  dex older than the control sample within at least  $1 R_e$  when we remove the effects of the  $g - r$  color.

We further select a new control sample adopting the stellar mass and  $g - r$  color in the whole galaxy as our primary selection criteria. The color criterium is

$$|(g - r)_{\text{AGN}} - (g - r)_{\text{ctr}}| \leq 0.05, \quad (10)$$

where  $(g - r)_{\text{AGN}}$  and  $(g - r)_{\text{ctr}}$  represent the  $g - r$  colors in the AGN and control samples, respectively. For each AGN, we select the control galaxy which meeting the mass and color criteria. Similar with the situation in Section 2.1.2, for each AGN, there might be more than one normal dwarf galaxy meeting the above criteria, and thus for those matched sources we further limit its redshift based on equation (3). Finally, we choose the one with the closest match in  $g - r$  color if there are still more than one matched objects.

In Figure 11, we show  $\langle \log t_{\star} \rangle_L$  profiles for the AGN and new color-selected control samples, respectively. The median values of  $\langle \log t_{\star} \rangle_L$  for the new control sample are about 9.0 in  $0-1 R_e$  and larger than 9.0 in  $1-2 R_e$ . The stellar ages of new color-selected control sample are younger than AGN sample, especially in the  $0-1 R_e$ , with differences ranging from  $\sim 0.3$  dex to  $\sim 0.5$  dex. In the outer region, the differences of the stellar age tend to be small. Therefore, for these BPT-selected AGN-host dwarf galaxies, although the differences of the stellar age between the AGN and control samples become smaller when we consider the selection effect, the stellar ages within at least  $1 R_e$  are still  $\sim 0.3$  dex to  $\sim 0.5$  dex older than those of control galaxies. This is agreement with our previous conclusion that AGN might cause the old stellar age in dwarf galaxy by accelerating the consumption of the cold gas, but limited to the inner region.

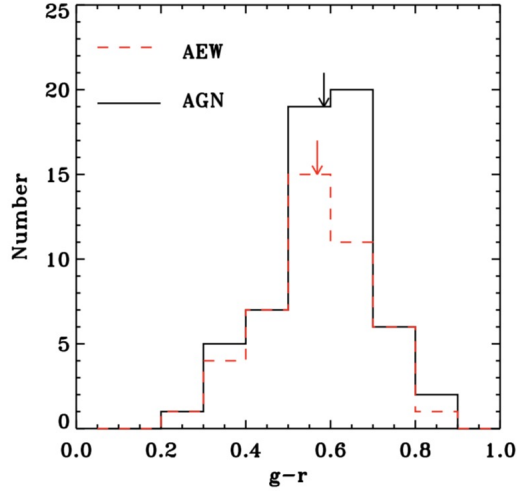


Fig. 12: Number distributions of  $g-r$  color for the AGN sample and the AGN sample with  $EW(H\alpha) > 3\text{\AA}$ . The black solid line and red dashed line represent the AGN sample and the AGN sample with  $EW(H\alpha) > 3\text{\AA}$ , respectively. Arrows represent the median values of the  $g-r$  color.

#### 4.2 The $H\alpha$ equivalent width of the AGN sample

The AGN sample is selected according to the BPT diagram, which might cause the selected AGN dwarf galaxies are not true AGNs. A series of works (e.g., Binette et al. 1994; Sarzi et al. 2010; Cid Fernandes et al. 2011; Papaderos et al. 2013; Singh et al. 2013) have argued that the low-mass hot evolved stars might be the emission sources of the harder ionization field, which could be mistaken for AGN. The criteria ( $H\alpha$  equivalent width,  $EW(H\alpha) > 3\text{\AA}$ ) suggested by Cid Fernandes et al. (2011) are used to check if the selected AGN candidates are true AGNs. For the 49 AGN candidates identified by the spatially resolved BPT diagram, we re-construct the spatially resolved BPT diagram for those spaxels with  $S/N > 3$  and  $EW(H\alpha) > 3\text{\AA}$  and find that 40 sources are true AGNs. Further, for the 11 AGNs added by using the central  $1''.5$  radius spectra, there exist 5 galaxies having  $EW(H\alpha) > 3\text{\AA}$ , as shown in Table 1.

The  $g-r$  color distribution of these 45 AGN candidates meeting  $EW(H\alpha) > 3\text{\AA}$  is shown in Figure 12. The median value of the  $g-r$  color is 0.57, which is still redder than the control sample (0.44). Therefore, the red  $g-r$  color of AGN sample is not caused by mistaking the low-mass hot evolved stars in the center as the AGN. The selected AGN dwarf galaxies according to BPT diagram are indeed red galaxies. We further checked the co-added radial properties for these 45 AGN candidates and found that the stellar age and metallicity profiles have no significant change, as shown in Table 2.

## 5 SUMMARY

We search AGNs using BPT diagram among a parent sample including about 900 dwarf galaxies from MaNGA with stellar mass less than  $5 \times 10^9 M_\odot$ . We derive the spatial resolved stellar populations with STARLIGHT code and construct the radial stellar age/metallicity profiles for this AGN sample. In order to investigate AGN effects on dwarfs, we further compare the co-added radial properties of the AGN sample with those of a control sample. Our main results are summarized as follows:

1. The median values of the co-added light-weighted mean stellar age for the AGN sample are as old as 2–3 Gyr within  $2 R_e$ , while for the control sample, the median values of the co-added light-weighted mean stellar age range from  $3 \times 10^8$  to  $10^9$ yr, which are about 3–7 times younger than the AGN sample. This indicates that these AGN-host dwarfs are almost quiescent due to the lack of gas. Further, most of our AGN candidates are low-level AGNs, as only one objects have its  $L_{[\text{O III}]}$   $\geq 10^7 L_\odot$ . This is consistent with the old stellar age of the AGN-host dwarf galaxies, as the AGNs also become weak due to the lack of gas.
2. The co-added mass-weighted mean stellar age profiles for the AGN and control samples are both almost flat within  $2 R_e$ . Meanwhile, the median values of the co-added mass-weighted mean stellar age for the AGN and control samples are both about 10 Gyr within  $2 R_e$ , which suggests the stellar masses of these dwarf galaxies are mainly contributed by the old populations. For the control sample, the co-added light-weighted mean stellar age profile shows a ‘U’ shape curve with a negative gradient (-0.12) in the inner region and a positive gradient (0.31) in the outer region. However, the co-added light-weighted mean stellar age profile for the AGN sample is almost flat within  $2 R_e$ .
3. For both the AGN and control samples, the  $\nabla_{t_L}$  and  $\nabla_{x_Y}$  in  $0-0.5 R_e$ ,  $0.5-1 R_e$  and  $0-1 R_e$  almost have no correlation with the galaxy morphology.
4. The co-added light-weighted standard deviation of the log age with  $2 R_e$  are in the range of 0.3–0.8 (1.0–1.2) for the AGN (control) sample, while the co-added mass-weighted standard deviation of the log age have a much narrower range (0.2–0.4) for both sample, suggesting that these dwarf galaxies experience a continuous star-forming activities, but the stellar mass is assembled within a short period of time.
5. The co-added mean stellar metallicity profiles have a decreasing trend with increasing radius for both sample, and the similar mean stellar metallicity profiles for both samples indicate that AGNs have no strong impact on the chemical evolution of the host galaxy.

**Acknowledgements** We thank the anonymous referee for a careful reading and thoughtful comments which improved the paper. We thank Dr. Zhang Hong-Xin for a thorough reading of the paper and the useful suggestions which have improved the paper. The work is supported by the National Key R&D Program of China grant No. 2017YFA0402704, the Natural Science Foundation of China (NSFC; grant Nos. 11991051, 11421303 and 11973039), and the CAS Pioneer Hundred Talents Program. The STARLIGHT project is supported by the Brazilian agencies CNPq, CAPES, and FAPESP and by the France–Brazil CAPES/Cofecub program. All the authors acknowledge the work of the Sloan Digital Sky Survey (SDSS) team. Funding for SDSS- IV has been provided by the Alfred P. Sloan Foundation and Participating Institutions. Additional funding towards SDSS-IV has been provided by the US Department of Energy Office of Science. SDSS-IV acknowledges support and resources from the Centre for High-Performance Computing at the University of Utah. The SDSS web site is [www.sdss.org](http://www.sdss.org). SDSS-IV is managed by the Astrophysical Research Consortium for the Participating Institutions of the SDSS Collaboration including the Brazilian Participation Group, the Carnegie Institution for Science, Carnegie Mellon University, the Chilean Participation Group, the French Participation Group, Harvard–Smithsonian Center for Astrophysics, Instituto de Astrofísica de Canarias, The Johns Hopkins University, Kavli

Institute for the Physics and Mathematics of the Universe (IPMU)/University of Tokyo, Lawrence Berkeley National Laboratory, Leibniz Institut für Astrophysik Potsdam (AIP), Max-Planck-Institut für Astronomie (MPIA Heidelberg), Max-Planck-Institut für Astrophysik (MPA Garching), Max-Planck-Institut für Extraterrestrische Physik (MPE), National Astronomical Observatory of China, New Mexico State University, New York University, University of Notre Dame, Observatório Nacional/MCTI, The Ohio State University, Pennsylvania State University, Shanghai Astronomical Observatory, United Kingdom Participation Group, Universidad Nacional Autónoma de México, University of Arizona, University of Colorado Boulder, University of Oxford, University of Portsmouth, University of Utah, University of Virginia, University of Washington, University of Wisconsin, Vanderbilt University and Yale University.

## References

- Andrews, B. H., & Martini, P. 2013, *ApJ*, 765, 140
- Asari, N. V., Cid Fernandes, R., Stasińska, G., et al. 2007, *MNRAS*, 381, 263
- Baldwin, J. A., Phillips, M. M., & Terlevich, R. 1981, *PASP*, 93, 5
- Barai, P., & de Gouveia Dal Pino, E. M. 2019, *MNRAS*, 487, 5549
- Barden, M., Rix, H.-W., Somerville, R. S., et al. 2005, *ApJ*, 635, 959
- Barth, A. J., Ho, L. C., Rutledge, R. E., & Sargent, W. L. W. 2004, *ApJ*, 607, 90
- Bellovary, J. M., Cleary, C. E., Munshi, F., et al. 2019, *MNRAS*, 482, 2913
- Bellovary, J., Volonteri, M., Governato, F., et al. 2011, *ApJ*, 742, 13
- Binette, L., Magris, C. G., Stasińska, G., & Bruzual, A. G. 1994, *A&A*, 292, 13
- Birchall, K. L., Watson, M. G., & Aird, J. 2020, *MNRAS*, 492, 2268
- Blanton, M. R., Bershady, M. A., Abolfathi, B., et al. 2017, *AJ*, 154, 28
- Bower, R. G., Benson, A. J., Malbon, R., et al. 2006, *MNRAS*, 370, 645
- Bradford, J. D., Geha, M. C., Greene, J. E., Reines, A. E., & Dickey, C. M. 2018, *ApJ*, 861, 50
- Bruzual, G., & Charlot, S. 2003, *MNRAS*, 344, 1000
- Bundy, K., Bershady, M. A., Law, D. R., et al. 2015, *ApJ*, 798, 7
- Cai, W., Zhao, Y., Zhang, H.-X., Bai, J.-M., & Liu, H.-T. 2020, *ApJ*, 903, 58
- Calzetti, D., Armus, L., Bohlin, R. C., et al. 2000, *ApJ*, 533, 682
- Calzetti, D., Kinney, A. L., & Storchi-Bergmann, T. 1994, *ApJ*, 429, 582
- Cardelli, J. A., Clayton, G. C., & Mathis, J. S. 1989, *ApJ*, 345, 245
- Chen, G., Zhang, H.-X., Kong, X., et al. 2020, *ApJ*, 895, 146
- Cheung, E., Bundy, K., Cappellari, M., et al. 2016, *Nature*, 533, 504
- Cid Fernandes, R., Gu, Q., Melnick, J., et al. 2004, *MNRAS*, 355, 273
- Cid Fernandes, R., Mateus, A., Sodré, L., Stasińska, G., & Gomes, J. M. 2005, *MNRAS*, 358, 363
- Cid Fernandes, R., Stasińska, G., Mateus, A., & Vale Asari, N. 2011, *MNRAS*, 413, 1687
- Dashyan, G., Silk, J., Mamon, G. A., Dubois, Y., & Hartwig, T. 2018, *MNRAS*, 473, 5698
- Drory, N., MacDonald, N., Bershady, M. A., et al. 2015, *AJ*, 149, 77
- Fabian, A. C. 2012, *ARA&A*, 50, 455
- Ferrarese, L., & Merritt, D. 2000, *ApJ*, 539, L9

- Filippenko, A. V., & Sargent, W. L. W. 1989, *ApJ*, 342, L11
- Gebhardt, K., Bender, R., Bower, G., et al. 2000, *ApJ*, 539, L13
- González Delgado, R. M., García-Benito, R., Pérez, E., et al. 2015, *A&A*, 581, A103
- Heckman, T. M., & Best, P. N. 2014, *ARA&A*, 52, 589
- Hinshaw, G., Weiland, J. L., Hill, R. S., et al. 2009, *ApJS*, 180, 225
- Kauffmann, G., White, S. D. M., Heckman, T. M., et al. 2004, *MNRAS*, 353, 713
- Kauffmann, G., Heckman, T. M., Tremonti, C., et al. 2003, *MNRAS*, 346, 1055
- Kewley, L. J., Dopita, M. A., Sutherland, R. S., Heisler, C. A., & Trevena, J. 2001, *ApJ*, 556, 121
- Kormendy, J., & Ho, L. C. 2013, *ARA&A*, 51, 511
- Koski, A. T. 1978, *ApJ*, 223, 56
- Koudmani, S., Sijacki, D., Bourne, M. A., & Smith, M. C. 2019, *MNRAS*, 484, 2047
- Law, D. R., Yan, R., Bershad, M. A., et al. 2015, *AJ*, 150, 19
- Law, D. R., Cherinka, B., Yan, R., et al. 2016, *AJ*, 152, 83
- Le Borgne, J. F., Bruzual, G., Pelló, R., et al. 2003, *A&A*, 402, 433
- Lemons, S. M., Reines, A. E., Plotkin, R. M., Gallo, E., & Greene, J. E. 2015, *ApJ*, 805, 12
- Mallmann, N. D., Riffel, R., Storchi-Bergmann, T., et al. 2018, *MNRAS*, 478, 5491
- Manzano-King, C. M., Canalizo, G., & Sales, L. V. 2019, *ApJ*, 884, 54
- Mateo, M. L. 1998, *ARA&A*, 36, 435
- Mateus, A., Sodr e, L., Cid Fernandes, R., et al. 2006, *MNRAS*, 370, 721
- Mezcua, M., & Dom nguez S nchez, H. 2020, *ApJ*, 898, L30
- Mezcua, M., Suh, H., & Civano, F. 2019, *MNRAS*, 488, 685
- Moran, E. C., Shahinyan, K., Sugarman, H. R., V lez, D. O., & Eracleous, M. 2014, *AJ*, 148, 136
- Morelli, L., Corsini, E. M., Pizzella, A., et al. 2015, *MNRAS*, 452, 1128
- O'Donnell, J. E. 1994, *ApJ*, 422, 158
- Papaderos, P., Gomes, J. M., V lchez, J. M., et al. 2013, *A&A*, 555, L1
- Penny, S. J., Masters, K. L., Weijmans, A.-M., et al. 2016, *MNRAS*, 462, 3955
- Penny, S. J., Masters, K. L., Smethurst, R., et al. 2018, *MNRAS*, 476, 979
- Reines, A. E., Condon, J. J., Darling, J., & Greene, J. E. 2020, *ApJ*, 888, 36
- Reines, A. E., Greene, J. E., & Geha, M. 2013, *ApJ*, 775, 116
- Rembold, S. B., Shimoia, J. S., Storchi-Bergmann, T., et al. 2017, *MNRAS*, 472, 4382
- Riffel, R., Pastoriza, M. G., Rodr guez-Ardila, A., & Bonatto, C. 2009, *MNRAS*, 400, 273
- Ro kar, R., Debattista, V. P., Stinson, G. S., et al. 2008, *ApJ*, 675, L65
- Ruiz-Lara, T., P rez, I., Florido, E., et al. 2016, *MNRAS*, 456, L35
- Salpeter, E. E. 1955, *ApJ*, 121, 161
- S nchez, S. F., Avila-Reese, V., Hernandez-Toledo, H., et al. 2018, *RMxAA*, 54, 217
- Sartori, L. F., Schawinski, K., Treister, E., et al. 2015, *MNRAS*, 454, 3722
- Sarzi, M., Shields, J. C., Schawinski, K., et al. 2010, *MNRAS*, 402, 2187
- Schaye, J., Crain, R. A., Bower, R. G., et al. 2015, *MNRAS*, 446, 521
- Schlegel, D. J., Finkbeiner, D. P., & Davis, M. 1998, *ApJ*, 500, 525



- Sellwood, J. A., & Binney, J. J. 2002, *MNRAS*, 336, 785
- Sharma, R. S., Brooks, A. M., Somerville, R. S., et al. 2020, *ApJ*, 897, 103
- Silk, J. 2017, *ApJ*, 839, L13
- Singh, R., van de Ven, G., Jahnke, K., et al. 2013, *A&A*, 558, A43
- Smee, S. A., Gunn, J. E., Uomoto, A., et al. 2013, *AJ*, 146, 32
- Storchi-Bergmann, T., González Delgado, R. M., Schmitt, H. R., Cid Fernandes, R., & Heckman, T. 2001, *ApJ*, 559, 147
- Terrazas, B. A., Bell, E. F., Pillepich, A., et al. 2020, *MNRAS*, 493, 1888
- Trebitsch, M., Volonteri, M., Dubois, Y., & Madau, P. 2018, *MNRAS*, 478, 5607
- Tremonti, C. A., Heckman, T. M., Kauffmann, G., et al. 2004, *ApJ*, 613, 898
- Trump, J. R., Sun, M., Zeimann, G. R., et al. 2015, *ApJ*, 811, 26
- Veilleux, S., & Osterbrock, D. E. 1987, *ApJS*, 63, 295
- Wuyts, S., Förster Schreiber, N. M., van der Wel, A., et al. 2011, *ApJ*, 742, 96
- Yan, R., Bundy, K., Law, D. R., et al. 2016a, *AJ*, 152, 197
- Yan, R., Tremonti, C., Bershady, M. A., et al. 2016b, *AJ*, 151, 8
- Zhang, H.-X., Hunter, D. A., Elmegreen, B. G., Gao, Y., & Schruba, A. 2012, *AJ*, 143, 47
- Zhao, Y., Gu, Q., & Gao, Y. 2011, *AJ*, 141, 68
- Zheng, Z., Thilker, D. A., Heckman, T. M., et al. 2015, *ApJ*, 800, 120
- Zheng, Z., Wang, H., Ge, J., et al. 2017, *MNRAS*, 465, 4572